Title:

On the Origin of Directional Variability in Earthquake Response Spectra: A Stochastic Covariance Framework

Authors:

Rajesh Rupakhety[1]

Víctor M. Hernández-Aguirre[2]

[1] Earthquake Engineering Research Centre, Faculty of Civil and Environmental Engineering, University of Iceland, Austurvegur 2a, 800 Selfoss, Iceland

Email: rajesh@hi.is

[2] Earthquake Engineering Research Centre, Faculty of Civil and Environmental Engineering, University of Iceland, Austurvegur 2a, 800 Selfoss, Iceland

Email: victorh@hi.is

Preprint Statement

This manuscript is a preprint and has been accepted in Earthquake Engineering and Structural Dynamics

The final and published article is available at

https://onlinelibrary.wiley.com/doi/10.1002/eqe.70287.

On the Origin of Directional Variability in Earthquake Response Spectra: A Stochastic Covariance Framework

Rajesh Rupakhety[1]*, Victor Moises Hernández-Aguirre[1]

Abstract

Directional variability of horizontal earthquake response spectra is commonly characterized using rotation-based measures such as RotD50 and RotD100, yet the stochastic mechanisms underlying this variability remain incompletely understood. This study develops a covariance-based framework for directional oscillator response under isotropic excitation. A geometric anisotropy measure, κ_{rms}, is defined from the normalized eigenvalue contrast of the two-component response covariance matrix. Under independent isotropic Gaussian sampling, κ_{rms}^2 is the complement of the classical bivariate sphericity statistic and follows an exact Beta distribution. The trace–anisotropy formulation used here recovers this classical result directly in coordinates relevant to directional oscillator response. For temporally correlated and amplitude-modulated oscillator response, the independent-sample law is used as a stochastic baseline through an effective-sample-size closure relating anisotropy to oscillator bandwidth, energetic duration, and period. Monte Carlo simulations verify this approximation under controlled conditions, while analysis of a large set of real ground motion records shows systematic period- and duration-dependent covariance anisotropy consistent with finite-sample covariance effects. The results further demonstrate that RotD100/RotD50 is not a direct measure of anisotropy: covariance anisotropy develops before peak extraction, upon which directional peak-selection effects subsequently act. The framework therefore provides a stochastic covariance baseline against which additional physical directionality in recorded motions may be interpreted.

Keywords: directionality, response spectra, covariance anisotropy, effective sample size, polarization, sphericity

1. Introduction

Directional variability of horizontal earthquake ground motion is a well-documented phenomenon. Response spectral ordinates depend on orientation, and the ratio of the maximum to the median spectral ordinate across all non-redundant horizontal orientations, RotD100/RotD50 (Boore, 2010), is consistently greater than one across observed ground-motion databases. This ratio exhibits systematic dependence on oscillator period and shaking duration (Boore and Kishida, 2017; Shahi and Baker, 2014). Using stochastic simulations, Poulos et al. (2021) further demonstrated that directional variability persists even when the two horizontal components are generated from the same isotropic stochastic process. These studies established several important empirical observations, but a theoretical framework explaining the origin of the phenomenon, its governing distribution, and its controlling parameter has remained absent.

Addressing this gap is important not only for understanding the origin of directional variability, but also for its practical interpretation in earthquake engineering. Directional effects have become increasingly important in record selection (Nievas and Sullivan, 2018), seismic assessment (Nievas and Sullivan, 2017; Skoulidou et al., 2019), and loss estimation (Feng et al., 2021; Lagaros, 2010). Such applications motivate a clearer distinction between directional variability arising intrinsically from finite-duration stochastic response and that associated with persistent physical directionality in the ground motion.

To understand where such a framework enters, it is useful to recall the structure of random vibration theory (RVT) for univariate processes. In RVT, the peak response of a linear oscillator is expressed as the product

[1] Earthquake Engineering Research Centre, Faculty of Civil and Environmental Engineering, University of Iceland, Austurvegur 2a, 800 Selfoss, Iceland, rajesh@hi.is

* Corresponding author

of an RMS (root mean square) response level and a peak factor. The RMS response is determined by the second-order statistics of the response process, whereas the peak factor accounts for the stochastic occurrence of extremes within a finite duration (Cartwright and Longuet-Higgins, 1956; Vanmarcke, 1972). This separation between covariance structure and peak generation underpins the interpretation of earthquake response spectra.

Extending this decomposition to horizontal directional response requires an additional geometric layer. The two horizontal components of linear-oscillator response define a bivariate random process whose covariance matrix possesses two principal variances, represented by its eigenvalues $\lambda_1 \geq \lambda_2$. These define a response ellipse in the horizontal plane. The shape of this ellipse characterises the directional structure of the RMS response before peak selection occurs. The directional spectrum, obtained by taking maxima of directional projections of the response process, introduces a second source of variability associated with peak selection.

This observation suggests a natural bivariate analogue of the univariate RVT decomposition. Directional spectral variability may be viewed as the combination of covariance anisotropy, associated with the geometry of the response ellipse, and peak-factor anisotropy, associated with directional fluctuations of extremes. The latter has recently been shown to form a smooth, low-dimensional stochastic field over orientation, dominated by the lowest admissible angular harmonic (Rupakhety and Hernández-Aguirre, 2026). The present study develops the stochastic structure of the covariance component and retains the peak-factor contribution explicitly in the directional response-field formulation. This separation allows covariance-driven anisotropy to be identified and studied independently before examining how peak selection subsequently modifies the directional spectral field.

Even when the underlying excitation is perfectly isotropic, the covariance matrix estimated from a finite record will generally not be isotropic. Finite-sample fluctuations produce unequal covariance eigenvalues and hence a non-circular RMS response ellipse. Under independent Gaussian sampling, the statistics of the sample covariance matrix are governed by the Wishart distribution (Muirhead, 2009). In classical multivariate analysis, the corresponding isotropic population condition is known as the sphericity hypothesis, and the exact null distribution of the associated bivariate shape statistic was established by Mauchly (1940).

To express this covariance geometry in a form directly relevant to directional response spectra, we define the geometric anisotropy measure

$$\kappa_{\mathrm{rms}} = \frac{\lambda_1 - \lambda_2}{\lambda_1 + \lambda_2}, \qquad \lambda_1 > \lambda_2 \tag{1}$$

where λ_1 and λ_2 are the eigenvalues of the covariance matrix of the two-component pseudo-acceleration response. Pseudo-acceleration response here is defined as the relative displacement response multiplied by the squared circular frequency. The quantity κ_{rms} is a bounded, scale-invariant measure of covariance shape: it is zero for an isotropic response and approaches unity as the covariance becomes increasingly concentrated along a single direction. Just as the RMS level σ in univariate RVT characterises the scale of response prior to peak selection, κ_{rms} characterises the shape of the bivariate response prior to peak selection.

The choice of κ_{rms} is both geometrically natural and mathematically convenient. Its square is the complement of the classical bivariate sphericity statistic. Consequently, under independent isotropic Gaussian sampling,

$$\kappa_{\mathrm{rms}}^2 \sim \mathrm{Beta}\left(1, \frac{N - 1}{2}\right)$$

where N denotes the Wishart degrees of freedom. Section 3 recovers this classical bivariate sphericity result directly from the real Wishart eigenvalue density and expresses it in trace–anisotropy coordinates suited to directional oscillator response.

The independent-sample result provides a natural stochastic baseline, but oscillator response histories are temporally correlated and therefore do not supply one independent covariance realization per recorded time step. To connect the classical finite-sample result to filtered oscillator response, we introduce an effective sample size N_{eff} and use the corresponding Beta family as an effective-sample-size closure. The quantity links covariance uncertainty to engineering parameters through the temporal correlation structure of the oscillator response. For filtered and amplitude-modulated response, a first-order approximation shows that scales with the ratio of an effective energetic duration to oscillator period. Within this approximation, the observed period and duration dependences of directional anisotropy arise as different manifestations of the same reduction in the number of effective covariance realizations.

The geometric significance of κ_{rms} extends beyond the RMS field itself. The directional PSA (pseudo spectral acceleration) field can be expressed as a multiplicative combination of the RMS response ellipse and a stochastic directional peak-factor field. This leads naturally to a relationship connecting covariance-based anisotropy to PSA-based anisotropy, thereby providing a bridge between the underlying covariance geometry and commonly used rotation-invariant intensity measures such as RotD50 and RotD100.

The contributions of this paper are fourfold. First, we formulate bivariate oscillator response as the combination of a covariance-defined RMS geometry and a distinct directional peak-factor modulation, thereby separating second-order anisotropy from peak-selection effects. Second, we identify the normalized eigenvalue contrast κ_{rms} as a natural measure of this covariance geometry and establish its exact correspondence with the classical bivariate sphericity statistic, expressing the associated finite-sample law in trace–anisotropy coordinates suited to directional response analysis. Third, we introduce an effective-sample-size closure that connects this independent-sample baseline to temporally correlated and amplitude-modulated oscillator response. Fourth, using Monte Carlo simulations and a large strong-motion dataset, we examine how finite covariance sampling contributes to the observed dependence of directional anisotropy on oscillator period and response duration.

The paper is organised as follows. Section 2 introduces the directional response-field representation and the covariance-based anisotropy measure κ_{rms}. Section 3 establishes its connection to classical bivariate sphericity and recovers the corresponding finite-sample Beta law directly from the isotropic Wishart eigenvalue density. Section 4 develops the effective-degrees-of-freedom framework for filtered and amplitude-modulated response. Then, Section 5 presents Monte Carlo verification and Section 6 evaluates the proposed framework against a large population of recorded ground motions. Section 7 discusses implications for directional response spectra and directional ground-motion modelling, and Section 8 presents the conclusions.

2. Directional Response Field and Anisotropy Invariants

2.1 RMS covariance and geometric anisotropy

Let $\mathbf{a}(t) \in \mathbb{R}^2$ denote the two horizontal components of the pseudo-acceleration response process of a linear oscillator at fixed period T. Here, pseudo-acceleration response process refers to the oscillator response time history obtained by multiplying the relative displacement response by the squared circular frequency of the oscillator. It should be distinguished from pseudo-spectral acceleration (PSA), which is defined subsequently as the maximum absolute value of the response process over time. For a direction $\theta \in [0, \pi)$, the directional response is defined as

$$a(t, \theta) = \mathbf{u}(\theta)^\top \mathbf{a}(t), \qquad \mathbf{u}(\theta) = \begin{pmatrix} \cos\theta \\ \sin\theta \end{pmatrix} \tag{2}$$

The second-order geometry of the response process is described by its covariance matrix

$$\mathbf{C} = \mathbb{E}\left[\mathbf{a}(t)\mathbf{a}(t)^\top\right] \tag{3}$$

and the directional second moment (variance) is

$$\sigma_a^2(\theta) = \mathbb{E}[a(t, \theta)^2] = \mathbf{u}(\theta)^\top \mathbf{C} \mathbf{u}(\theta) \tag{4}$$

Let $\lambda_1 \geq \lambda_2 \geq 0$ denote the eigenvalues of $\mathbf{C}$, and let θ_0 be the eigenvector direction corresponding to λ_1. The directional RMS field admits the exact representation,

$$\sigma_a^2(\theta) = \bar{\sigma}_a^2[1 + \kappa_{\mathrm{rms}} \cos 2(\theta - \theta_0)] \tag{5}$$

where

$$\bar{\sigma}_a^2 = \frac{\lambda_1 + \lambda_2}{2}, \quad \kappa_{\text{rms}} = \frac{\lambda_1 - \lambda_2}{\lambda_1 + \lambda_2}, \qquad 0 \leq \kappa_{\text{rms}} \leq 1 \tag{6}$$

Eq. (5) shows that the covariance matrix defines an elliptical second-order response geometry in the horizontal plane (Flinn, 1965). The quantity $\bar{\sigma}_a^2$ controls the overall scale of the ellipse, whereas κ_{rms} controls its shape. When κ_{rms} is 0, the ellipse reduces to a circle and the RMS response is isotropic. As κ_{rms} approaches unity, the ellipse becomes increasingly elongated, corresponding to progressively stronger directional anisotropy. Because it depends only on the eigenvalue structure of the covariance matrix, it characterizes the directional geometry of the RMS response independently of subsequent peak selection. Geometric interpretations of directional response fields based on elliptical structure have previously been proposed for rotation-invariant spectral measures (Rupakhety, 2026). The present work adopts a covariance-based formulation and develops its stochastic implications.

2.2 Directional PSA and multiplicative structure

Directional pseudo-spectral acceleration is defined as

$$\text{PSA}(\theta) = \max_t \mid a(t,\theta) \mid \tag{7}$$

The directional peak factor is defined as

$$p(\theta) = \frac{\text{PSA}(\theta)}{\sigma_a(\theta)} \tag{8}$$

To separate the overall peak-factor level from its directional fluctuations, the logarithmic peak-factor field can be written as (Rupakhety and Hernández-Aguirre, 2026)

$$\ln p(\theta) = \mu_p + \varepsilon(\theta) \tag{9}$$

where μ_p denotes the median logarithmic peak factor and $\varepsilon(\theta)$ is a π-periodic fluctuation field with zero median over $[0,\pi)$. Thus, μ_p controls the median level of the directional peak-factor field, while $\varepsilon(\theta)$ captures directional deviations from that level. Defining the squared PSA field, $S(\theta) = \text{PSA}^2(\theta)$, and substituting the peak-factor representation of Eq. (9) yields

$$S(\theta) = \text{PSA}^2(\theta) = \sigma_a^2(\theta)\exp(2\mu_p)\exp(2\varepsilon(\theta)) \tag{10}$$

Using the elliptical RMS form from Eq. (5) gives

$$S(\theta) = C[1 + \kappa_{\text{rms}}\cos 2(\theta - \theta_0)]\exp(2\varepsilon(\theta)) \tag{11}$$

where $C = \bar{\sigma}_a^2\exp(2\mu_p)$. Eq. (11) expresses the directional PSA field as the product of two distinct components: a geometric covariance-driven term governed by κ_{rms}, and a stochastic peak-factor term governed by $\varepsilon(\theta)$. This multiplicative representation forms the basis for the anisotropy decomposition developed in the following section.

2.3 Symmetric–antisymmetric decomposition

To isolate the contribution of peak-factor fluctuations to directional anisotropy, the peak-factor field is decomposed into components that are symmetric and antisymmetric with respect to a rotation of $\pi/2$

$$\varepsilon^s(\theta) = \frac{\varepsilon(\theta) + \varepsilon(\theta + \pi/2)}{2}, \varepsilon^a(\theta) = \frac{\varepsilon(\theta) - \varepsilon(\theta + \pi/2)}{2} \tag{12}$$

It follows that $\varepsilon(\theta) = \varepsilon^s(\theta) + \varepsilon^a(\theta)$, $\varepsilon(\theta + \pi/2) = \varepsilon^s(\theta) - \varepsilon^a(\theta)$. The symmetric component ε^s is preserved under a $\pi/2$ rotation and therefore contributes equally to the two members on an orthogonal pair. The antisymmetric component ε^a changes sign under a rotation of $\pi/2$ and therefore controls their directional contrast. Evaluating the squared field from Eq. (11) in the RMS principal frame ($\theta_0 = 0$) at the orthogonal pair $\theta = (0, \pi/2)$ yields

$$S(0) = C(1+\kappa_{\mathrm{rms}})\exp\big(2(\varepsilon^s+\varepsilon^a)\big) \text{ and } S(\pi/2) = C(1-\kappa_{\mathrm{rms}})\exp(2(\varepsilon^s-\varepsilon^a)) \tag{13}$$

The corresponding PSA anisotropy invariant, quantifying normalized contrast in the RMS principal directions, is defined as

$$\kappa_{\mathrm{psa}} = \frac{S(0)-S(\pi/2)}{S(0)+S(\pi/2)} \tag{14}$$

Substituting $S(0)$ and $S(\pi/2)$ from Eq. (13) in Eq. (14) and using the identity $tanh(z) = \frac{\exp(2z)-1}{\exp(2z)+1}$, one obtains

$$\kappa_{\mathrm{psa}} = \frac{\kappa_{\mathrm{rms}} + \tanh(2\varepsilon^a)}{1+\kappa_{\mathrm{rms}}\tanh(2\varepsilon^a)} \tag{15}$$

Thus, κ_{psa} is a fractional-linear, or Möbius, transformation of κ_{rms}. Eq. (15) establishes a direct connection between covariance-based anisotropy and PSA-based anisotropy. The quantity κ_{rms} depends only on the geometry of the response covariance matrix, whereas κ_{psa} contains an additional contribution associated with peak selection. The fractional-linear form shows that peak-factor fluctuations enter through the antisymmetric component ε^a, while the symmetric component cancels identically. Consequently, κ_{rms} may be interpreted as the underlying geometric anisotropy of the oscillator response, whereas κ_{psa} is the corresponding anisotropy observed in directional PSA.

3. Distribution of Geometric Anisotropy Under Isotropic Excitation

3.1 Finite-sample covariance of isotropic Gaussian response

To identify the intrinsic stochastic component of directional anisotropy, consider an idealized two-component pseudo-acceleration response process at a fixed oscillator period (*T*), denoted by

$$\mathbf{X}(t) = \begin{bmatrix} X_1(t) \\ X_2(t) \end{bmatrix} \tag{16}$$

The process is assumed to be zero-mean, stationary, Gaussian, and second-order isotropic. Isotropy implies that the population covariance matrix is proportional to the identity,

$$\mathbb{E}[\mathbf{X}(t)\mathbf{X}(t)^\top] = \sigma^2\mathbf{I}_2 \tag{17}$$

so that no preferred direction exists in the population response. This defines the isotropic reference state used to quantify anisotropy generated solely by finite covariance sampling. In classical multivariate analysis, the same covariance condition is referred to as the sphericity hypothesis (Mauchly, 1940). To first establish the independent-sample reference problem, consider *N* statistically independent vector realizations $\mathbf{X}^{(i)}, i = 1, \dots, N$, from this isotropic Gaussian population, with $X^{(i)} \sim \mathcal{N}_2(0, \sigma^2 I_2)$. Their sample covariance matrix is

$$\hat{C} = \frac{1}{N}\sum_{i=1}^{N} X^{(i)}\, X^{(i)\top} \tag{18}$$

Under the Gaussian assumption, the scaled matrix $N\hat{\mathbf{C}}$ follows a two-dimensional Wishart distribution (Muirhead, 2009),

$$N\hat{\mathbf{C}} \sim \mathcal{W}_2(N, \sigma^2\mathbf{I}_2) \tag{19}$$

The Wishart distribution is the multivariate analogue of the chi-squared distribution. Just as the sample variance of N independent Gaussian scalars fluctuates around its population value, the sample covariance matrix of N independent Gaussian vectors fluctuates around the isotropic covariance $\sigma^2\mathbf{I}_2$. Consequently, although the population covariance possesses no preferred orientation, the sample covariance matrix will generally have unequal eigenvalues. Finite covariance sampling therefore generates realization-dependent directional anisotropy even when the underlying population is perfectly isotropic.

3.2 The anisotropy coordinate and bivariate sphericity

Let $\lambda_1 \geq \lambda_2 > 0$ denote the ordered eigenvalues of the sample covariance matrix $\hat{\mathbf{C}}$. As shown in Section 2, directional anisotropy is naturally characterized by the normalized eigenvalue contrast κ_{rms} defined in Eq. (6). To separate covariance magnitude from covariance shape, define the trace variable

$$s = \lambda_1 + \lambda_2 \tag{20}$$

The eigenvalues may then be written as

$$\lambda_1 = \frac{s}{2}(1 + \kappa_{\text{rms}}), \qquad \lambda_2 = \frac{s}{2}(1 - \kappa_{\text{rms}}) \tag{21}$$

The variable s represents the total variance contained in the covariance estimate, whereas κ_{rms} represents its geometric anisotropy. The anisotropy coordinate is directly related to the classical bivariate sphericity statistic. From Eq. (21),

$$1 - \kappa_{\text{rms}}^2 = \frac{4\lambda_1\lambda_2}{(\lambda_1 + \lambda_2)^2} = \frac{\det \hat{\mathbf{C}}}{\left[\text{tr}(\hat{\mathbf{C}})/2\right]^2} \tag{22}$$

The right-hand side is the bivariate form of the classical sphericity statistic. In Mauchly's (1940) formulation, the corresponding ellipticity statistic is its square root. Thus, κ_{rms}^2 and the classical sphericity statistic are complementary one-to-one measures of normalized covariance shape: the former increases with anisotropy, whereas the latter decreases with departure from sphericity.

The choice of κ_{rms} remains particularly useful for directional response analysis. It is bounded and scale invariant, and directly characterizes normalized covariance shape independently of the total response level s. The variables λ_1 and λ_2 jointly encode both covariance magnitude and anisotropy, whereas the transformation to (s, κ_{rms}) separates these two aspects explicitly. This makes κ_{rms}, rather than the individual eigenvalues themselves, the natural variable for studying directional covariance anisotropy.

A formally analogous normalized eigenvalue contrast appears in optical and radar polarimetry as the degree of polarization of a 2×2 Hermitian coherency matrix. That literature generally concerns complex Wishart matrices and different physical estimators, but it provides a mathematically adjacent interpretation of normalized covariance anisotropy (Touzi and Lopes, 1996).

3.3 Exact Beta law for covariance anisotropy

For the isotropic Wishart distribution of the sample covariance matrix, the joint probability density of the ordered eigenvalues is (Muirhead, 2009)

$$f(\lambda_1, \lambda_2) \propto (\lambda_1\lambda_2)^{((N-3)/2)}(\lambda_1 - \lambda_2)\exp[-N(\lambda_1 + \lambda_2)/(2\sigma^2)] \tag{23}$$

Introducing the eigenvalue contrast $d = \lambda_1 - \lambda_2$ and transforming from (λ_1, λ_2) to (s, d) coordinates yields

$$f(s, d) \propto \left(\frac{s^2 - d^2}{4}\right)^{(N-3)/2} d \exp\left(-\frac{Ns}{2\sigma^2}\right) \tag{24}$$

with domain $s > 0$ and $0 \leq d \leq s$. Substituting $d = s\kappa_{\text{rms}}$ gives

$$f(s, \kappa_{\text{rms}}) \propto s^{N-1} \exp\left(-\frac{Ns}{2\sigma^2}\right) \kappa_{\text{rms}}(1 - \kappa_{\text{rms}}^2)^{(N-3)/2} \tag{25}$$

Under the isotropic null, the trace variable s and the anisotropy variable κ_{rms} separate multiplicatively,

$$f(s, \kappa_{\text{rms}}) = f_s(s) f_\kappa(\kappa_{\text{rms}}) \tag{26}$$

where

$$f_s(s) \propto s^{N-1} \exp\left(-\frac{Ns}{2\sigma^2}\right) \tag{27}$$

and

$$f_\kappa(\kappa_{\text{rms}}) \propto \kappa_{\text{rms}}(1 - \kappa_{\text{rms}}{}^2)^{(N-3)/2} \tag{28}$$

is the marginal density of κ_{rms}. This factorisation is the bivariate expression of the classical separation between covariance scale and normalized covariance shape under the sphericity hypothesis. In the present formulation, it is useful because it isolates the distribution of directional shape from the overall response amplitude. The distribu/tion of κ_{rms} can therefore be obtained without further reference to the trace variable. When the population covariance departs from isotropy, covariance scale and normalized anisotropy are generally coupled and the factorization no longer applies in the same form. The corresponding independent-sample non-null problem is nevertheless classical; Girshick (1941) derived the distribution of Mauchly's ellipticity statistic when the sphericity hypothesis is false.

Defining $y = \kappa_{\mathrm{rms}}^2$, and applying the change-of-variables formula $f(y) = f(\kappa_{\mathrm{rms}})|d\kappa_{\mathrm{rms}}/dy|$, with $\kappa_{\mathrm{rms}} = \sqrt{y}$ and $d\kappa_{\mathrm{rms}}/dy = 1/(2\sqrt{y})$, the Jacobian exactly cancels the leading $\sqrt{y}$ factor in Eq. (28), yielding

$$f(y) \propto (1-y)^{(N-3)/2};\ 0 \le \mathrm{y} \le 1 \tag{29}$$

Recognizing the Beta-distribution kernel and normalizing yields

$$\kappa_{\mathrm{rms}}^2 \sim \mathrm{Beta}\left(1, \frac{N-1}{2}\right) \tag{29}$$

Under perfectly isotropic Gaussian condition, the squared covariance anisotropy therefore follows an exact Beta distribution governed solely by the number of statistically independent realizations *N*.

Eq. (29) is equivalent to Mauchly's (1940) exact bivariate null distribution under the transformation in Eq. (22). The apparent one-degree-of-freedom difference in sample-size notation arises from the treatment of the process mean: Mauchly estimates the mean from the observations, yielding Wishart degrees of freedom, whereas the present formulation assumes a known zero mean and therefore gives degrees of freedom. The derivation above therefore does not introduce a new bivariate Wishart distribution. Rather, it recovers the classical bivariate sphericity result directly from the real Wishart eigenvalue density and expresses it in trace–anisotropy coordinates suited to directional oscillator response.

Some special cases are instructive. When $N = 3$, the distribution of κ_{rms}^2reduces to $\mathrm{Beta}(1,1)$ corresponding to a uniform distribution on $[0,1]$. As *N* increases, the distribution progressively concentrates near zero, reflecting convergence of the sample covariance matrix toward its isotropic population value. Equation (30) provides the exact independent-sample baseline used in the remainder of the paper. Section 4 develops an effective-degrees-of-freedom closure for applying this baseline approximately to temporally correlated and amplitude-modulated oscillator response.

3.4 Moments and geometric interpretation

The Beta distribution immediately yields exact expressions for the moments of geometric anisotropy. The second moment is

$$\mathbb{E}[\kappa_{\mathrm{rms}}^2] = \frac{2}{N+1} \tag{30}$$

The mean and variance of the distribution are

$$\mathbb{E}[\kappa_{\mathrm{rms}}] = \frac{(N-1)\sqrt{\pi}}{4} \frac{\Gamma\left(\frac{N-1}{2}\right)}{\Gamma\left(\frac{N}{2}+1\right)} \quad \text{and} \quad \mathrm{Var}(\kappa_{\mathrm{rms}}) = \mathbb{E}[\kappa_{\mathrm{rms}}^2] - (\mathbb{E}[\kappa_{\mathrm{rms}}])^2 \tag{31}$$

where $\Gamma(\cdot)$ denotes the Gamma function. For large *N*, Stirling's approximation gives

$$\mathbb{E}[\kappa_{\mathrm{rms}}] \approx \sqrt{\frac{\pi}{2N}},\ \ \mathrm{Var}(\kappa_{\mathrm{rms}}) \approx \frac{4-\pi}{2N} \quad \text{and} \quad \mathrm{sd}(\kappa_{\mathrm{rms}}) \approx \sqrt{\frac{4-\pi}{2N}} \tag{32}$$

Both the mean and standard deviation therefore decay as $N^{-1/2}$. The characteristic magnitude of covariance anisotropy decreases only slowly with increasing sample size, implying that appreciable directional anisotropy may persist even when the underlying excitation is perfectly isotropic. Further insight is obtained by examining the large-*N* limit. Writing $y = \kappa_{\mathrm{rms}}^2$, the Beta density satisfies

$$f_y(y) \propto (1-y)^{(N-3)/2} \approx e^{-Ny/2} \tag{33}$$

for small *y*. Consequently, $N\kappa_{\mathrm{rms}}^2$ converges to an exponential distribution with mean 2, and $\sqrt{N}\kappa_{\mathrm{rms}}$ converges to a Rayleigh distribution with unit scale. The statistical result has a direct geometric interpretation. The population covariance ellipse is circular and possesses no distinguished axis. The sample covariance matrix is a random perturbation of this circular state: its principal eigenvector identifies a randomly oriented direction in the plane, while κ_{rms} quantifies the anisotropy of the resulting sample ellipse. By symmetry, the principal direction is uniformly distributed over $[0, \pi)$, whereas the squared anisotropy magnitude follows the Beta distribution of Eq. (30). The emergence of directional structure under an isotropic ensemble is therefore not paradoxical. It is an inevitable consequence of finite-sample covariance estimation. A perfectly isotropic process observed over a finite duration will generally produce a non-circular sample covariance ellipse. The distribution of its anisotropy is governed by *N* alone.

4. Oscillator Memory and Effective Degrees of Freedom

4.1 Effective degrees of freedom for covariance estimation

Section 3 derived the exact distribution of geometric anisotropy for a covariance matrix estimated from *N* statistically independent realizations of a zero-mean, stationary, Gaussian, and second-order isotropic process. For oscillator response time histories, however, successive samples are temporally correlated, so the number of recorded time samples is not the relevant covariance sample size. We therefore introduce an effective covariance sample size by matching the variance of the covariance estimator for the correlated process to that of the independent-sample Wishart reference problem.

Let $X(t)$ and $Y(t)$ be independent, zero-mean, stationary Gaussian processes with common variance σ^2 and normalized autocorrelation function $\rho(\tau)$, where $\rho(0) = 1$. Consider the continuous-time sample cross-covariance estimator over an observation window of duration *D*,

$$\widehat{C_{XY}} = \frac{1}{D} \int_0^D X(t) Y(t) \, dt \tag{34}$$

Because covariance anisotropy is determined by fluctuations of the sample covariance matrix, the relevant sampling scale can be identified from the variance of its covariance estimators. Using Isserlis' theorem for fourth-order Gaussian moments, together with independence and zero mean of $X(t)$ and $Y(t)$, the variance of the covariance estimator is

$$\mathrm{Var}\left(\widehat{C_{XY}}\right) = \frac{\sigma^4}{D^2} \int_0^D \int_0^D \rho^2(t - s) \, dt \, ds \tag{35}$$

Because the integrand depends only on the time difference $\tau = t - s$, Eq. (36) can be rewritten as

$$\mathrm{Var}\left(\widehat{C_{XY}}\right) = \frac{\sigma^4}{D^2} \int_{-D}^{D} (D - |\tau|) \rho^2(\tau) \, d\tau \tag{36}$$

The weighting factor $(D - |\tau|)$ reflects the finite observation window: large time lags contribute less because fewer sample pairs are available. If the record duration is large compared with the correlation decay scale of the process, then $\rho^2(\tau)$ is negligible for most values of $|\tau|$ approaching D. Over the region where the integrand contributes appreciably, the weighting factor may therefore be approximated by *D*, giving

$$\mathrm{Var}\left(\widehat{C_{XY}}\right) \approx \frac{\sigma^4}{D} \int_{-\infty}^{\infty} \rho^2(\tau) \, d\tau \tag{37}$$

Since the autocorrelation function is even, i.e., $\rho(-\tau) = \rho(\tau)$, it follows that

$$\mathrm{Var}\left(\widehat{C_{XY}}\right) \approx \frac{\sigma^4}{D} \, 2 \int_0^{\infty} \rho^2(\tau) \, d\tau \tag{38}$$

For N independent Gaussian realizations, the corresponding Wishart covariance variance is σ^4/N. Matching this variance to Eq. (39) defines the effective sample size

$$N_{\mathrm{eff}} \approx \frac{D}{2\int_0^\infty \rho^2(\tau)\, d\tau} \tag{39}$$

Equation (40) shows that the effective covariance sample size is controlled by the integral of the squared autocorrelation function. Stronger temporal correlation increases this integral and therefore reduces N_{eff}. The quantity N_{eff} should thus be interpreted as a variance-equivalent number of independent covariance realizations, not as the actual number of independent samples contained in the record.

4.2 SDOF filtering and period scaling

For a linear SDOF oscillator, filtering changes the temporal correlation structure of the response. Consider the pseudo-acceleration response of an oscillator with natural frequency $\omega_n = 2\pi/T$ and damping ratio ξ, subjected to broadband Gaussian input. For lightly damped response, the process is narrowband around the oscillator frequency and its normalized autocorrelation is approximated by

$$\rho(\tau) \approx e^{-\alpha|\tau|}\cos(\omega_d \tau) \tag{40}$$

where $\alpha = \xi\omega_n$ and $\omega_d \approx \omega_n\sqrt{1-\xi^2}$. Substitution $\rho(\tau)$ into Eq. (40) requires the integral of $\rho^2(\tau)$. Using the identity $\cos^2(\omega_d\tau) = [1+\cos(2\omega_d\tau)]/2$, and retaining the leading term for lightly damped response, gives $\int_0^\infty \rho^2(\tau)\, d\tau \approx 1/4\alpha$. Hence from Eq. (40) we obtain

$$N_{\mathrm{eff}} \approx 2\alpha D = 2\xi\omega_n D = \frac{4\pi\xi D}{T} \tag{41}$$

Equation (42) shows that, within the present narrowband approximation, longer-period oscillators have longer correlation times and therefore smaller variance-equivalent covariance sample sizes for a fixed duration. Substituting this expression into Eq. (30) gives

$$\kappa_{\mathrm{rms}}^2(T) \sim \mathrm{Beta}\left(1, \frac{N_{\mathrm{eff}}(T)-1}{2}\right) \tag{42}$$

Using the large-N_{eff} approximation from Section 3, Eq. (33) then gives

$$\mathbb{E}[\kappa_{\mathrm{rms}}(T)] \approx \sqrt{\frac{T}{8\xi D}} \tag{43}$$

Thus, within the narrowband and variance-matching approximations used here, the characteristic covariance anisotropy increases approximately as the square root of oscillator period for fixed damping and duration.

4.3 Amplitude non-stationarity and energetic effective duration

The preceding derivation assumes stationary response over a finite observation window of duration *D*. Real earthquake records are non-stationary: their energy is concentrated within a limited part of the record and modulated by an evolving amplitude envelope. To represent this effect in a mathematically tractable way, consider an amplitude-modulated process $g_i(t) = w(t)u_i(t)$ where $u_i(t)$ are stationary Gaussian processes and $w(t)$ is a deterministic envelope. The envelope is assumed to vary slowly relative to the correlation time of the underlying filtered process. Repeating the variance-matching argument for the covariance estimator gives

$$N_{\mathrm{eff}} = \frac{\left(\int w^2(t)\, dt\right)^2}{\int w^4(t)\, dt}\frac{1}{2\int_0^\infty \rho^2(\tau)\, d\tau} \tag{44}$$

This expression naturally defines an energetic effective duration,

$$D_{\mathrm{eff}} = \frac{\left(\int w^2(t)\, dt\right)^2}{\int w^4(t)\, dt} \tag{45}$$

The quantity D_{eff} is the effective temporal support of the squared signal amplitude. It equals the full observation duration for a constant envelope and decreases as the signal energy becomes more concentrated in time. Unlike conventional duration measures, D_{eff} arises directly from the variance of the covariance estimator. Combining this duration with the SDOF autocorrelation approximation gives

$$N_{\text{eff}}(T) \approx \frac{4\pi\xi D_{\text{eff}}}{T} \tag{46}$$

Thus, within the amplitude-modulated formulation, concentration of response energy in time reduces the variance-equivalent covariance sample size and increases the characteristic magnitude and dispersion of κ_{rms}. This formulation represents amplitude modulation only; simultaneous evolution of frequency content or bandwidth would make the response correlation structure itself time dependent and is not captured by the stationary-carrier approximation used here.

4.4 Remarks on non-Gaussianity

The exact finite-*N* Beta law presented in Section 3 relies on Gaussianity, because only in that case is the sample covariance matrix Wishart distributed. For a general non-Gaussian bivariate process, the sample covariance matrix is no longer Wishart, and the exact factorisation of the joint density into trace and anisotropy coordinates need not hold. Therefore, the Beta law should be understood as the exact isotropic Gaussian baseline, not as a universal finite-sample distribution for all non-Gaussian processes.

Nevertheless, two observations clarify why the covariance-anisotropy baseline may remain robust in practice. First, κ_{rms} is invariant to any common amplitude scaling of the record. Consider a Gaussian scale-mixture process of the form $g_i(t) = \sqrt{V}\, u_i(t)$, where $u_i(t)$ are the components of an isotropic Gaussian process and $V > 0$ is a random amplitude factor that is common to the whole record and independent of $u_i(t)$. The sample covariance matrix is then

$$\widehat{\mathbf{C}_g} = V\widehat{\mathbf{C}_u} \tag{47}$$

Both eigenvalues are multiplied by the same factor V, and hence $\kappa_{\text{rms}}(g) = \kappa_{\text{rms}}(u)$. Record-level Gaussian scale mixtures may thus produce strongly non-Gaussian marginal amplitudes while leaving the normalized covariance anisotropy unchanged. The same invariance persists after linear filtering and deterministic envelope modulation because any common scalar factor cancels from the normalized eigenvalue contrast.

Second, when non-Gaussianity acts at the sample level rather than as a common record-level amplitude factor, the exact invariance no longer holds. A useful large-*N* result can nevertheless be obtained for a rotationally isotropic population with finite fourth radial moment. Writing each independent sample in polar form as $X_i = R_i \cos\Theta_i$ and $Y_i = R_i \sin\Theta_i$, with Θ_i uniform on $[0,2\pi)$ and independent of R_i, define the traceless covariance components

$$a = \frac{\widehat{C_{11}} - \widehat{C_{22}}}{2} = \frac{1}{2N}\sum_{i=1}^{N} R_i^2 \cos(2\Theta_i)\,, \qquad b = \widehat{C_{12}} = \frac{1}{2N}\sum_{i=1}^{N} R_i^2 \sin(2\Theta_i) \tag{48}$$

By the multivariate central limit theorem,

$$\sqrt{N}(a,b) \Rightarrow \mathcal{N}\left(0, \frac{E[R^4]}{8}\mathbf{I}_2\right) \tag{49}$$

where $\Rightarrow$ denotes convergence in distribution. Since the isotropic scale estimate $\hat{m} = (\widehat{C_{11}} + \widehat{C_{22}})/2$ converges in probability to σ^2, the large-*N* limit of the anisotropy statistic is

$$N\kappa_{\text{rms}}^2 \Rightarrow \gamma_4 \chi_2^2, \qquad \gamma_4 = \frac{\mathbb{E}[R^4]}{8\sigma^4} \tag{50}$$

Equation (51) generalizes the large-*N* isotropic Gaussian result of section 3. In Section 3, Eq. (34) showed that the large-*N* limit of the exact Beta distribution approaches an exponential density in the scaled variable $N\kappa_{rms}^2$, which is equivalent to a χ_2^2 distribution. Equation (51) shows that, for a rotationally isotropic non-

Gaussian process with finite fourth moment, the same asymptotic structure is preserved, but with an additional scale factor γ_4 determined by the fourth radial moment. For the Gaussian case, $\mathbb{E}[R^4] = 8\sigma^4$, giving $\gamma_4 = 1$, and Eq. (51) reduces exactly to the asymptotic limit implied by Eq. (34). More generally, $\gamma_4 > 1$ inflates the characteristic anisotropy, while $\gamma_4 < 1$ reduces it. To first order, this effect may therefore be interpreted as a renormalization of the effective number of covariance realizations,

$$N_{\text{eff}} \to \frac{N_{\text{eff}}}{\gamma_4} \tag{51}$$

Thus, to leading order, rotationally isotropic sample-level non-Gaussianity preserves the same asymptotic covariance-anisotropy structure while rescaling its characteristic magnitude relative to the Gaussian baseline.

It is important to note, however, that this correction applies only to sample-level non-Gaussianity. As discussed previously, a large class of non-Gaussian processes generated through record-level amplitude mixing leaves κ_{rms} unchanged because the common amplitude factor cancels from the normalized eigenvalue contrast. Consequently, the effect of non-Gaussianity on covariance anisotropy is not determined solely by marginal kurtosis, but also by the way the non-Gaussianity is introduced. In the present study, the Gaussian Beta law is therefore retained as an analytically tractable isotropic baseline. Non-Gaussian effects may enter either through an effective rescaling of covariance sampling or as departures from the Gaussian isotropic reference, depending on the structure by which non-Gaussianity arises.

4.5 Scope of the effective-degrees-of-freedom approximation

It is important to distinguish the exact independent-sample result from the analytical closure used for N_{eff}. The Beta law presented in Section 3 is the distributional result for covariance anisotropy under the isotropic Gaussian null. The expressions $N_{\text{eff}} \approx 4\pi\xi D/T$ and $N_{\text{eff}} \approx 4\pi\xi D_{\text{eff}}/T$ are analytically tractable first-order approximations for the variance-equivalent covariance sample size of filtered and non-stationary response.

The narrowband autocorrelation model and the slowly varying envelope approximation are therefore not assumptions of the Beta law itself. They enter only through the estimate of N_{eff}. Their purpose here is to expose the scaling implied by covariance estimation: oscillator period, damping, and effective duration influence anisotropy through the number of variance-equivalent covariance realizations. At very long periods, when only a few effective response cycles are present, or when the envelope varies on a time scale comparable to the response correlation time, these approximations may require correction. Alternative numerical, simulation-based, or empirical estimates of can be used within the same isotropic covariance baseline. The role of the closed-form expressions above is therefore to provide a transparent first-order scaling relation, not a population-level predictive model for real ground motions.

5. Verification and robustness

The analytical developments of Sections 3 and 4 are examined using Monte Carlo simulations of progressively more realistic excitation models. The simulations proceed from stationary isotropic Gaussian excitation filtered through a linear SDOF oscillator, to non-stationary enveloped excitation, and finally to the complete distribution of κ_{rms}^2. The objective is to assess how accurately the effective-degrees-of-freedom closure reproduces the covariance-anisotropy statistics generated by temporally correlated and amplitude-modulated oscillator response.

5.1 Stationary SDOF-filtered response

The first verification considers isotropic stationary Gaussian excitation filtered through a linear SDOF oscillator. For each oscillator period, 5000 independent two-component realizations were generated, and the corresponding covariance matrices and anisotropy measures were computed from the pseudo-acceleration response histories.

Figure 1 compares the simulated mean and standard deviation of $\kappa_{rms}(T)$ with the prediction obtained from the approximation $N_{\text{eff}} \approx 4\pi\xi D/T$. The agreement is close across the investigated period range. Both the mean and the variability of κ_{rms} increase systematically with oscillator period, consistent with the reduction in variance-equivalent covariance sample size predicted by the narrowband approximation.

The corresponding RotD100/RotD50 ratios are shown in the right panel of Figure 1. The median ratio increases gradually with period, while the width of the 16–84% quantile band also increases. Although the analytical developments are formulated in terms of κ_{rms}, the resulting anisotropy manifests directly in commonly used engineering measures. At short periods, directional amplification remains non-negligible even when κ_{rms} is small, reflecting the influence of peak-factor fluctuations. At longer periods, the increasing covariance anisotropy contributes to the growth and broadening of the RotD100/RotD50 distribution. Thus, substantial directional amplification can arise under perfectly isotropic excitation through the combined effects of finite-sample covariance anisotropy and stochastic peak selection.

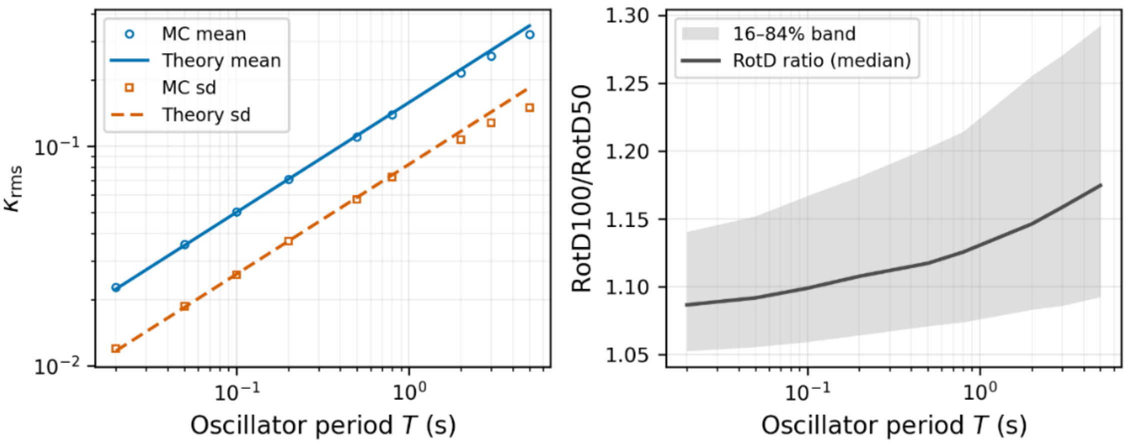

Figure 1. Monte Carlo verification of the SDOF-filtering closure. Left: ensemble mean and standard deviation of $\kappa_{rms}(T)$ compared with the theoretical scaling based on $N_{eff} \approx 4\pi\xi D/T$. Right: ensemble median and 16–84% quantile band of RotD100/RotD50 computed from 1° rotations of pseudo-acceleration response. 5000 simulations were run, each with a duration of 100s. Damping ratio is fixed at 5% of critical.

5.2 Non-stationary enveloped response

The second verification introduces amplitude non-stationarity through a smooth Gaussian amplitude envelope centred at the midpoint of the simulation window. The enveloped motions were filtered through the same SDOF oscillators and analysed using the covariance-based anisotropy measure.

Figure 2 compares the simulated anisotropy statistics with theoretical predictions obtained from the energetic duration D_{eff}. The solid curves correspond to the proposed model, while the dashed curves show the predictions obtained by replacing D_{eff} with the full record duration. The energetic-duration formulation reproduces the simulated mean and standard deviation of κ_{rms} accurately throughout most of the period range. In contrast, the stationary approximation systematically underestimates anisotropy because it overestimates the effective temporal support available for covariance estimation. The remaining discrepancies at the longest periods arise as the oscillator correlation time becomes comparable to the envelope width, where the slowly varying-envelope approximation begins to deteriorate.

The corresponding RotD100/RotD50 ratios are shown in the right panel of Figure 2. Relative to the stationary case, both the median ratio and the width of the 16-84% quantile band increase. The increase is consistent with the reduction in effective covariance sample size caused by concentrating the response energy within a shorter effective duration. RotD100/RotD50 ratios approaching 1.35 occur despite the underlying excitation remaining statistically isotropic, illustrating that substantial directional amplification can arise from the combined effects of finite-duration covariance anisotropy and stochastic peak selection even in the absence of persistent physical directionality.

The non-stationarity considered here is restricted to amplitude modulation of an otherwise stationary carrier. This isolates the effect of reduced effective covariance-sampling duration, but does not represent the full non-stationarity of earthquake ground motions, which may also exhibit time-varying dominant frequency and bandwidth. In such cases, the response correlation structure itself becomes time dependent. The present simulations therefore verify the effective-duration closure for amplitude-modulated excitation only; extension to jointly amplitude- and frequency-modulated processes lies outside the scope of this study.

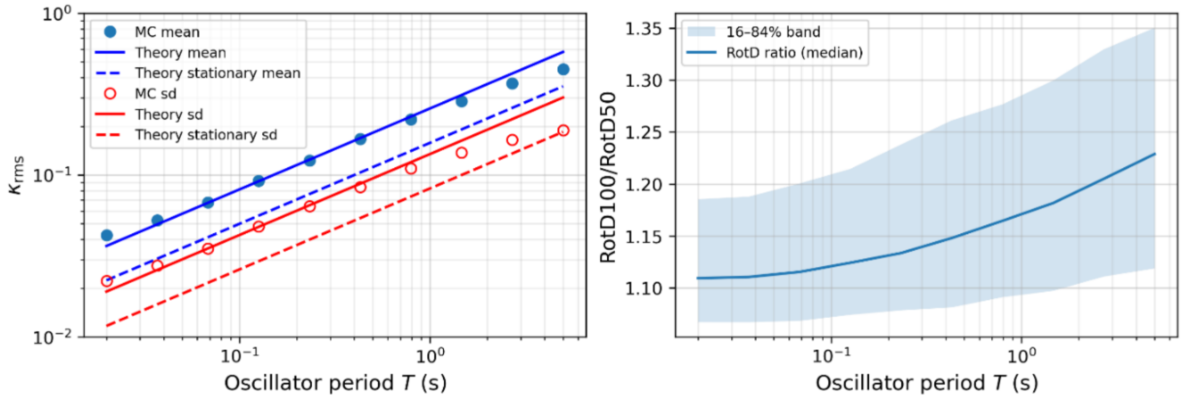

Figure 2. Monte Carlo verification of envelope-modified anisotropy. Left: ensemble mean and standard deviation of $\kappa_{rms}(T)$ from 5000 simulations of enveloped isotropic Gaussian excitation (total duration $D = 100s$, $dt = 0.005s$, $\xi =$ 5%), compared with theoretical predictions using the energetic effective duration D_{eff}(solid lines) and the full window length D(dashed lines). Right: median and 16–84% band of RotD100/RotD50 ratios obtained from the same simulations.

5.3 Verification of the full distribution

Figure 3 extends the verification to the complete distribution of κ_{rms}^2. Panel (a) considers independent Gaussian samples, for which the covariance matrix follows the classical Wishart distribution exactly. The simulated histogram agrees closely with the Beta distribution presented in Section 3, providing a direct numerical verification of the independent-sample result. Panel (b) considers stationary Gaussian excitation filtered through a linear SDOF oscillator. Although filtering introduces temporal correlation and reduces the variance-equivalent covariance sample size, the simulated distribution remains closely approximated by the same Beta family when parameterized by the effective degrees of freedom closure. Panel (c) further introduces amplitude modulation. The corresponding distribution is again well represented by the Beta approximation using the effective sample size associated with the energetic duration. These results indicate that, for the controlled excitation models considered here, temporal correlation and amplitude modulation affect covariance anisotropy primarily through the effective covariance sample size, while the Beta family provides an accurate approximation to the resulting distribution.

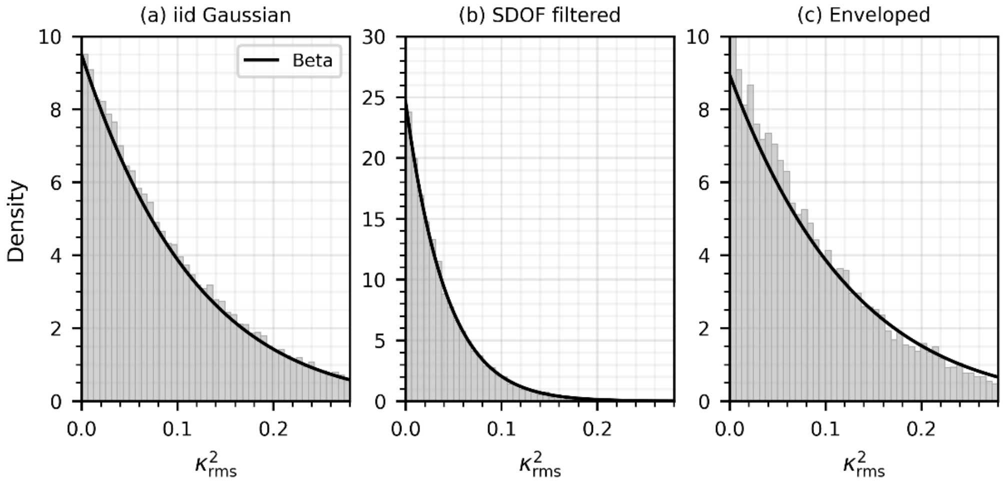

Figure 3. Empirical distributions of κ_{rms}^2 for three excitation models: (a) independent Gaussian samples, (b) stationary SDOF-filtered Gaussian response, and (c) SDOF-filtered enveloped Gaussian excitation. Histograms show simulated ensembles. Black curves denote the Wishart-derived Beta model. SDOF period is 0.5s and damping ratio is 5%.

5.4 Robustness to non-Gaussian excitation

The analytical results of Sections 3 and 4 use Gaussian assumptions at the level of the isotropic reference process and the Wishart covariance model. Real earthquake ground motions, however, may depart from

Gaussianity. To examine the sensitivity of the covariance-anisotropy framework to this assumption, Monte Carlo simulations were performed using non-Gaussian excitation carriers while retaining the same non-stationary envelope and oscillator filtering used in the preceding section.

The corresponding excess kurtosis values are 0.375, 1.0, and 6.0, respectively, representing progressively stronger departures from Gaussianity. The excitation histories were applied to a linear SDOF oscillator with damping ratio $\xi = 0.05$, and 50,000 independent realizations were generated for each combination of period and carrier distribution. For each realization, the covariance matrix of the two orthogonal pseudo-acceleration response components was computed and transformed into the covariance anisotropy measure κ_{rms}. The empirical distribution of κ_{rms}^2 obtained for each non-Gaussian carrier was then compared with the corresponding Gaussian-carrier distribution using the Kolmogorov–Smirnov distance, defined as the maximum absolute difference between their empirical cumulative distribution functions. Figure 4 shows the difference $\Delta F(x) = F_\nu(x) - F_G(x)$, where $F_G(x)$ denotes the empirical cumulative distribution function of κ_{rms}^2 obtained from the Gaussian carrier and $F_\nu(x)$ denotes that obtained from the Student-(t) carrier, for oscillator periods *T*=0.1, 0.5, 2, and 5 s. Across all periods, the deviations remain small and exhibit no systematic trend with increasing tail heaviness. Even for the t_5 carrier, whose excess kurtosis is six times larger than that of a Gaussian process, the resulting changes in the distribution of κ_{rms}^2 remain minor. The quantitative summary in Table 1 confirms this observation. The maximum Kolmogorov–Smirnov distance over all cases is less than 0.015, indicating that the cumulative distributions differ by less than approximately 1.5% at any point. Similarly, the mean value of κ_{rms}^2 changes by only a few percent relative to the Gaussian baseline. These results suggest that covariance anisotropy is controlled primarily by effective covariance sampling rather than by the marginal distribution of the excitation amplitudes. The influence of carrier non-Gaussianity is therefore secondary compared with the effects of oscillator memory and energetic duration that determine N_{eff}. Moreover, the differences tend to decrease with increasing oscillator period, consistent with the smoothing action of linear filtering, which progressively attenuates marginal non-Gaussianity in the response process. These simulations do not establish non-Gaussian invariance, but they indicate that the effective-sample-size Beta approximation is relatively insensitive to the tested Student-*t* carrier departures from Gaussianity.

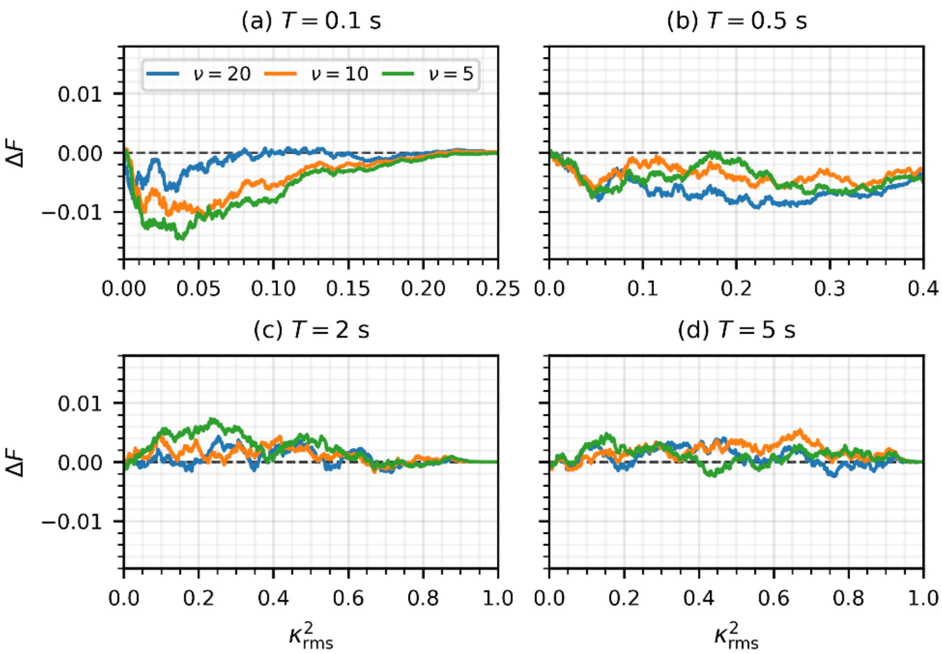

Figure 4. Differences between the empirical cumulative distributions of κ_{rms}^2 obtained from standardized Student-t carriers and the Gaussian-carrier baseline. Results are based on 50000 Monte Carlo simulations for $\xi = 5\%$. The small deviations demonstrate the robustness of the covariance anisotropy distribution to substantial carrier non-Gaussianity.

Table 1. Summary of robustness simulations using standardized Student-t carriers ($\nu = 20{,}10{,}5$). The theoretical effective sample size is computed from Eq. (47). The maximum excess kurtosis corresponds to the t_5 carrier. The maximum mean shift denotes the largest absolute percentage change in $\mathbb{E}[\kappa_{rms}^2]$ relative to the Gaussian-carrier

baseline. $D_{KS,max}$ denotes the maximum Kolmogorov–Smirnov distance between the empirical cumulative distributions obtained from the Gaussian and Student-t carriers.

Oscillator period T (s)	N_{eff}	Maximum excess kurtosis	Maximum mean shift (%)	$D_{KS,max}$
0.1	47.2	6.0	2.7	0.0146
0.5	9.45	6.0	1.4	0.0094
2.0	2.36	6.0	1.3	0.0073
5.0	0.94	6.0	0.3	0.0055

6. Comparison with recorded ground motions

The developments in Sections 3–5 established that geometric anisotropy arises intrinsically from finite-sample covariance fluctuations of filtered Gaussian processes. Real earthquake ground motions, however, differ from this idealization in several important respects. They are non-Gaussian, non-stationary, and may exhibit persistent directional structure associated with source radiation pattern (Kotha et al., 2019), directivity effects (Bradley and Baker, 2015), path heterogeneity (Campbell, 1991; Pischiutta et al., 2012), and local site-response effects (Burjánek et al., 2014; Vidale et al., 1991). Consequently, the applicability of the proposed stochastic framework to recorded motions is not self-evident and must be assessed empirically.

The analysis is based on 4690 horizontal-component recordings from the Engineering Strong Motion (ESM) database (Lanzano et al., 2021), corresponding to 417 earthquake events and 1304 recording stations. To ensure adequate signal quality and engineering relevance, only records from earthquakes with moment magnitude $M_w \geq 5$ and Joyner–Boore distance $R_{JB} \leq 200$ km were considered. The resulting dataset spans a broad range of source, path, and site conditions representative of strong-motion observations. Directional PSA fields were computed for 100 logarithmically spaced oscillator periods between 0.01 s and 10 s using 5% viscous damping. To avoid long-period filtering artefacts, periods exceeding $0.8/f_{hp}$ were excluded, where f_{hp} denotes the corner frequency of the high-pass filter applied during record processing.

Figure 5 compares the empirical cumulative distribution functions of κ^2_{rms} with the corresponding fitted Beta distributions at four representative oscillator periods. At each period, a single effective value of N_{eff} was estimated from the pooled observations by maximum likelihood. This comparison assesses whether the pooled empirical distribution is well represented by the one-parameter Beta family associated with the isotropic covariance baseline, independently of the analytical approximation used to estimate N_{eff}.

The adequacy of this single-Beta representation depends on oscillator period. At T=0.1 s, the Kolmogorov–Smirnov distance is D_{KS} ≈0.13. For a sample size of 4690, the nominal 5% critical value is approximately 0.020; thus, the hypothesis that the pooled short-period sample follows a single fitted Beta distribution is rejected. The discrepancy decreases substantially with increasing period, with D_{KS} approaching approximately 0.02 at T=5s, indicating that the practical approximation provided by a single Beta law improves markedly toward longer periods.

The short-period departure is consistent with the heterogeneity of the database. The Beta law applies conditionally for a specified covariance sample size, whereas the recordings have different durations, bandwidths, response correlation structures, and possibly different levels of persistent physical population anisotropy. Even under the isotropic-null closure alone, record-to-record variability in N_{eff} implies that the pooled distribution is a mixture of Beta distributions rather than a single Beta law.

The results also clarify the role of N_{eff} For a specified covariance sample size, the isotropic Gaussian baseline belongs to a one-parameter Beta family, whereas N_{eff} controls the characteristic magnitude of anisotropy and may vary substantially from one record to another. In principle, N_{eff} may be estimated empirically, inferred from stochastic simulations, or approximated from response duration and correlation structure. Figure 5 therefore shows that a single fitted Beta distribution can provide a useful effective description at intermediate and long periods, while a mixture of record-specific distributions is required for a more complete representation of the pooled population.

Poulos and Miranda (2022) observed that empirical distributions of PSA in a given direction normalized by RotD100 are well approximated by Beta distributions. The present results offer a possible structural explanation for why bounded Beta-like behaviour may emerge in directional response: covariance anisotropy itself follows a Beta family under the isotropic reference problem, while Eq. (15) shows how this covariance geometry is transformed by directional peak-factor modulation.

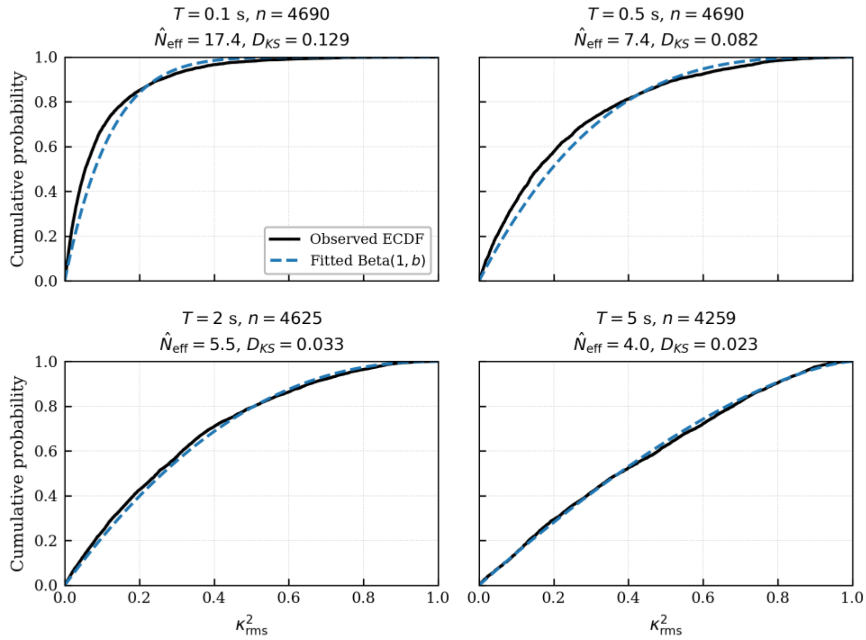

Figure 5. Empirical cumulative distribution functions of κ^2_{rms} for the ESM database at four representative oscillator periods. Black lines show observed distributions and blue dashed lines show fitted Beta distributions. The fitted effective sample size $\widehat{N}_{eff}$ and Kolmogorov–Smirnov distance D_{KS} are reported in each panel.

To examine the origin and variability of κ_{rms}, we next consider a simple first-order approximation based on response duration and oscillator period. Following Section 4, the effective covariance sample size is approximated as $N_{\mathrm{eff}}(T) \approx 4\pi\xi D_R^*(T)/\mathrm{T}$, where $D_R^*(T)$ denotes the energetic duration of the oscillator response. Strictly speaking, the theoretical derivation employs an effective duration associated with the modulation envelope of the process. In practical application, this envelope is unknown, and its effective duration is here approximated by the energetic duration computed directly from the oscillator response history.

To expose the role of duration at the population level, the recordings were divided into tertiles according to ground-motion energetic duration D_G^*. The resulting groups have median durations of approximately $D_G^* =$ 3.5, 8.4, and 17.3 s for the short-, intermediate-, and long-duration subsets, respectively. Figure 6 compares the observed median values of $\kappa_{\mathrm{rms}}(T)$ with the corresponding isotropic-null median predictions for the three duration groups. The right panel shows the associated median values of the conventional directional ratio RotD100/RotD50.

Several observations emerge. First, the recorded motions exhibit a clear and systematic duration dependence. Short-duration records display larger covariance anisotropy than long-duration records over most of the period range. The same ordering is evident in the RotD100/RotD50 ratio, showing that the duration dependence identified at the covariance level propagates into conventional engineering measures of directional response. This observation is consistent with earlier findings that directional amplification ratios depend on both oscillator period and duration (Poulos et al., 2021), but provides a different interpretation of the underlying mechanism. The observed duration dependence is also consistent with the mixture interpretation: even within the isotropic-null closure, pooling records with different durations combines populations associated with different effective covariance sample sizes.

Second, the isotropic-null model reproduces the observed duration ordering and captures a substantial fraction of the variation over the intermediate period range. This agreement is notable because the model contains no representation of rupture directivity, path effects, site amplification, or other persistent physical polarization mechanisms. The observed trends are therefore consistent with finite covariance sampling contributing materially to the directional anisotropy present in recorded motions.

Systematic departures from the prediction appear at both ends of the period range. At short periods, the approximation $N_{\mathrm{eff}}(T) \approx 4\pi\xi D_R^*(T)/\mathrm{T}$ implicitly assumes that the effective bandwidth of the response is controlled primarily by the oscillator. As oscillator period decreases, however, the response becomes increasingly transparent to the excitation and its bandwidth becomes constrained by the finite bandwidth of the ground motion itself. Consequently, the narrowband oscillator approximation can overestimate N_{eff} at short periods and therefore underpredict the corresponding covariance anisotropy.

At long periods, the discrepancy has a different origin. The approximation used to estimate N_{eff} follows from an asymptotic covariance-estimation argument in which the effective duration is large compared with the correlation time of the response. When only a few effective response cycles contribute to the covariance estimate, this asymptotic scaling becomes increasingly inaccurate and can underestimate the variance-equivalent covariance sample size. The resulting isotropic-null prediction therefore tends to overestimate anisotropy, particularly for short-duration records. Similar limitations of asymptotic random-vibration approximations in the few-cycle regime are well known and commonly motivate finite-window corrections.

The comparison therefore supports two distinct conclusions. First, the isotropic covariance framework provides a useful stochastic reference for interpreting covariance anisotropy in recorded earthquake motions. Second, the simple N_{eff} approximation captures much of the observed period and duration dependence over the intermediate period range but exhibits systematic biases at very short and very long periods. These discrepancies reflect limitations of the first-order effective-sample-size closure and may also contain contributions from departures of real ground motions from the isotropic-reference assumptions, including finite excitation bandwidth, more general non-stationarity, and persistent physical directionality.

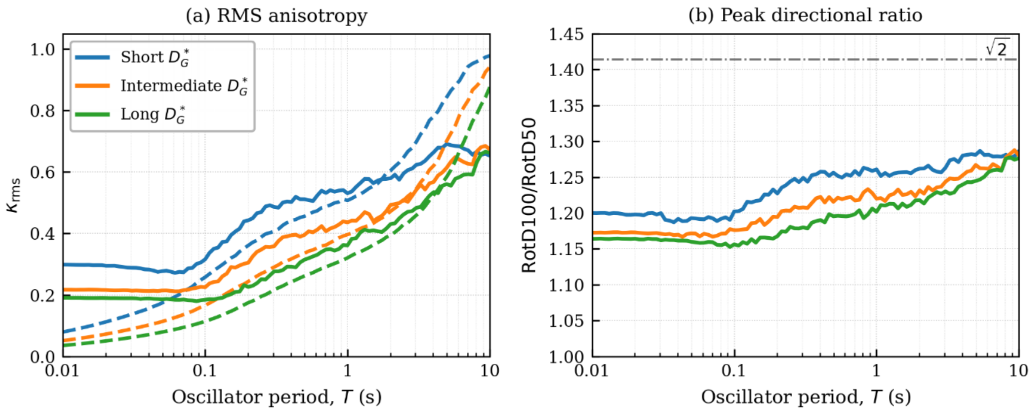

Figure 6. Comparison of observed and predicted directional anisotropy in the ESM database. Records were grouped into tertiles of ground-motion energetic duration D_G^*(median durations 3.5 s, 8.4 s, and 17.3 s). (a) Median covariance anisotropy $\kappa_{rms}(T)$. Solid lines show observations and dashed lines show stochastic predictions based on $N_{eff} = 4\pi\xi D_R^*(T)/T$. (b) Corresponding median values of $RotD100/RotD50$. The model reproduces the observed duration ordering and much of the period dependence over the intermediate period range.

7. Discussion

Directional variability of horizontal response spectra is commonly interpreted through rotation-based peak measures such as RotD100, RotD50, and ratios derived from them. Previous studies have shown that these quantities depend systematically on oscillator period and duration, and that non-negligible directional amplification can arise even when the two horizontal components are generated from the same isotropic stochastic process (Poulos et al., 2021). These findings established an important empirical fact: directional variability does not require a deterministic physical polarization mechanism. They also leave a more fundamental question, however: what part of the observed directionality is already present in the second-order geometry of the oscillator response, and what part is introduced by the stochastic selection of peaks?

The present results clarify this distinction. RotD100/RotD50 is not a direct measure of anisotropy of the directional response field, but a peak-based statistic combining at least two mechanisms: anisotropy of the oscillator-response covariance structure and directional variability associated with peak extraction. Covariance anisotropy exists before peak selection and produces a realization-dependent second-order response geometry quantified by κ_{rms}. Peak selection then acts on this underlying field and further modifies the directional distribution of spectral ordinates through the directional peak-factor field. Directional amplification and covariance anisotropy are therefore related but not equivalent. The former reflects the combined effects of covariance geometry and stochastic peak formation.

This distinction also clarifies the role of duration. Directional effects have previously been associated with finite-duration peak-factor mechanisms, such as the reduced number of opportunities for oscillators to attain large peaks in different orientations (Poulos et al., 2021). The present framework shows that finite duration acts earlier, at the covariance level. For a finite-duration filtered process, the sample covariance matrix fluctuates around its population value, producing unequal eigenvalues even when the population covariance is perfectly isotropic. The magnitude of this realization-level anisotropy depends on the amount of effectively independent covariance information contained in the response history. The governing first-order variable is therefore the variance-equivalent covariance sample size, rather than duration or oscillator period considered separately.

This interpretation unifies the observed period and duration dependences. Within the first-order closure developed here, the effective covariance sample size scales approximately with the ratio of energetic response duration to oscillator period. Increasing oscillator period or decreasing response duration therefore reduces effective covariance sampling and increases the expected magnitude of finite-sample anisotropy. Period dependence and duration dependence are consequently not independent phenomena within this mechanism, but different manifestations of the same reduction in effective covariance sampling. Records at the same oscillator period may therefore exhibit substantially different levels of covariance anisotropy when their response durations or bandwidths differ. Empirical directional models conditioned primarily on oscillator period may obscure this dependence by averaging over heterogeneous duration and bandwidth conditions.

The framework further clarifies the interpretation of preferred response directions. Recent studies have reported population-level tendencies for the orientation of maximum spectral response to align with physically meaningful directions, with stronger tendencies sometimes observed at long oscillator periods (Girmay et al., 2024). Such observations are physically important, but the direction associated with an individual record is meaningful only when the response field possesses sufficient anisotropy. When κ_{rms} is small, the covariance geometry is nearly isotropic and its principal direction is weakly constrained: a finite sample still produces a mathematically defined principal axis, but its orientation may be dominated by sampling fluctuations rather than by a persistent directional property of the underlying process. Peak-selection variability can introduce additional uncertainty in the orientation of the maximum spectral response. Conversely, when the observed anisotropy substantially exceeds the finite-sample isotropic baseline, the associated directional orientation becomes more plausibly attributable to persistent physical structure.

This issue is particularly relevant at long oscillator periods. Long-period response may exhibit stronger apparent directionality, but it is also characterized by fewer effective covariance realizations. The resulting increase in finite-sample anisotropy is accompanied by greater uncertainty in the orientation inferred from an individual realization. Thus, the period range in which preferred directions appear most pronounced can also be one in which record-level directional estimates are least stable. Population-level orientation trends may remain robust even when the dominant direction inferred from an individual short-duration, long-period response history is statistically uncertain. The isotropic covariance baseline therefore provides a context not only for interpreting the magnitude of observed anisotropy, but also for judging when an associated preferred direction is likely to carry physical information.

A further implication concerns the treatment of directional variability as aleatory uncertainty. For a given record, azimuthal variation is not an independent source of randomness. It is a structured field determined by the same two horizontal response histories. Rotation-based quantities such as RotD50, RotD100, arbitrary-component response, and component-to-component variability are therefore not separate physical objects; they are different summaries or projections of the same directional response field. The randomness across records lies instead in the descriptors of that field, including its overall response scale, covariance anisotropy, orientation, and directional peak-factor modulation. Treating component-to-component variability (Girmay and Miranda, 2026) as an additional independent scalar aleatory term may obscure the geometric coupling between directions and can implicitly treat different orientations of the same record as though they represented independent realizations.

The field view also clarifies the practical role of the present framework. A covariance-based representation characterizes the second-order geometry of the directional response directly. Once the overall response scale, covariance anisotropy, principal orientation, and directional peak-factor modulation are described, conventional rotation-based measures can in principle be obtained as derived quantities rather than introduced as separate stochastic objects. This perspective is consistent with the finding that the directional peak-factor fluctuation itself forms a smooth, low-dimensional stochastic field over orientation (Rupakhety and Hernández-Aguirre, 2026). Together, the covariance geometry and peak-factor modulation therefore provide a compact representation of the principal ingredients controlling the directional PSA field.

Such a representation offers a path toward directional ground-motion models that operate on the full angular response field rather than separately modelling selected scalar measures or percentile ratios. In that setting, an amplitude model would describe the overall response scale, the covariance model would describe anisotropy and orientation, and the peak-factor model would describe the remaining directional modulation associated with extreme response. Rotation-invariant quantities such as RotD50 and RotD100 would then arise as operators applied to the resulting field. This approach preserves the dependence between orientations and provides a natural basis for propagating directional response through applications such as record selection, conditional simulation, and seismic demand modelling without treating dense angular rotations as independent observations.

The distinction between stochastic covariance anisotropy and persistent physical directionality is equally important. The isotropic model developed here does not imply that source, path, or site mechanisms are unimportant. Rather, it shows that a non-circular response field is already expected from finite covariance sampling even in the absence of such mechanisms. Physical directionality should therefore be interpreted relative to this stochastic reference rather than relative to perfect circularity. Departures in anisotropy magnitude, orientation, or their joint behaviour beyond the isotropic baseline may then provide information about persistent source-, path-, or site-induced structure.

Thus, the main conceptual advance of this work is the separation of covariance geometry from peak response. Classical bivariate sphericity theory supplies the finite-sample distribution of covariance shape under independent isotropic Gaussian sampling; the present framework identifies this covariance anisotropy as a mechanism of directional oscillator response, embeds it within the RMS–peak-factor decomposition of response spectra, and separates it from the additional directional variability introduced by peak selection. The effective-sample-size formulation provides a first-order connection between this independent-sample baseline and finite-duration filtered response. In this view, directional variability is neither solely a peak-factor phenomenon nor necessarily evidence of persistent physical polarization: it emerges from the interaction of finite-sample covariance geometry, directional peak formation, and, in recorded motions, any additional physical directional structure present in the ground motion.

8. Conclusions

This paper developed a stochastic covariance framework for directional anisotropy of horizontal oscillator response. The normalized eigenvalue contrast $\kappa_{\mathrm{rms}} = (\lambda^1 - \lambda^2)/(\lambda^1 + \lambda^2)$ provides a bounded and scale-invariant measure of covariance shape. Its square is complementary to the classical bivariate sphericity statistic and, for N independent samples from an isotropic Gaussian population, follows the exact distribution $\kappa_{\mathrm{rms}}^2 \sim \mathrm{Beta}(1, (N-1)/2)$. The trace–anisotropy formulation used here recovers this classical result directly from the real Wishart eigenvalue density and expresses it in variables suited to directional oscillator response. The principal contribution of the present framework is therefore the identification of finite-sample covariance anisotropy as a mechanism of directional oscillator response and its separation from the additional directional variability introduced by peak selection.

To connect the independent-sample baseline to finite-duration oscillator response, a variance-equivalent effective sample size N_{eff} was introduced. For lightly damped, amplitude-modulated response, the first-order approximation $N_{\mathrm{eff}} \approx 4\pi\xi D_{\mathrm{eff}}/T$ relates covariance anisotropy to oscillator period, damping, and energetic duration. Monte Carlo simulations show close agreement between this closure and the simulated mean, dispersion, and distribution of κ_{rms} under stationary filtered and amplitude-modulated Gaussian excitation. Additional simulations with standardized Student-t carriers produced maximum Kolmogorov–Smirnov differences below 0.015 relative to the Gaussian-carrier distributions, indicating limited sensitivity to the forms of carrier non-Gaussianity examined here.

Analysis of 4690 ground motion records from 417 earthquakes and 1304 stations confirms systematic period- and duration-dependent covariance anisotropy. A single fitted Beta distribution does not describe the pooled population uniformly across period: the Kolmogorov–Smirnov distance is approximately 0.13 at *T* = 0.1 s, clearly rejecting a single-Beta representation, but decreases to approximately 0.023 at *T* = 5 s. This behaviour is consistent with a heterogeneous population containing record-specific effective covariance sample sizes rather than one common N_{eff}. When the records are separated into duration tertiles with median ground-motion energetic durations of approximately 3.5, 8.4, and 17.3 s, short-duration motions exhibit systematically greater κ_{rms} than long-duration motions over most of the period range. The same duration ordering is observed in RotD100/RotD50. The first-order N_{eff} approximation reproduces much of this ordering and period dependence over the intermediate-period range, while systematic departures remain at short and long periods.

These findings show that covariance anisotropy develops before peak extraction and is distinct from directional peak-factor variability. Rotation-based quantities such as RotD100/RotD50 consequently combine covariance geometry with stochastic peak-selection effects rather than measuring covariance anisotropy directly. More generally, non-zero realization-level anisotropy is expected even for an isotropic population because of finite covariance sampling. The isotropic covariance model therefore provides a stochastic reference against which persistent source-, path-, or site-induced directionality in recorded motions may be interpreted.

Acknowledgements

The constructive comments of the Editor, Dr. Iunio Iervolino, and two anonymous reviewers significantly improved the clarity and scope of the manuscript.

Data availability

All ground motion data used in this study are available at the Engineering Strong Motion Database (https://esm-db.eu/#/home)

Author contributions

RR: conceptual framework, mathematical derivation, modelling, coding, drafting and editing VMHA: data collection, processing, coding, drafting, and editing

References

Boore, D.M., 2010. Orientation-independent, nongeometric-mean measures of seismic intensity from two horizontal components of motion. Bull. Seismol. Soc. Am. 100, 1830–1835.

Boore, D.M., Kishida, T., 2017. Relations between some horizontal-component ground-motion intensity measures used in practice. Bull. Seismol. Soc. Am. 107, 334–343.

Bradley, B.A., Baker, J.W., 2015. Ground motion directionality in the 2010–2011 Canterbury earthquakes. Earthq. Eng. Struct. Dyn. 44, 371–384. https://doi.org/10.1002/eqe.2474

Burjánek, J., Edwards, B., Fäh, D., 2014. Empirical evidence of local seismic effects at sites with pronounced topography: a systematic approach. Geophys. J. Int. 197, 608–619. https://doi.org/10.1093/gji/ggu014

Campbell, K.W., 1991. An empirical analysis of peak horizontal acceleration for the Loma Prieta, California, earthquake of 18 October 1989. Bull. Seismol. Soc. Am. 81, 1838–1858. https://doi.org/10.1785/BSSA0810051838

Cartwright, D.E., Longuet-Higgins, M.S., 1956. The statistical distribution of the maxima of a random function. Proc. R. Soc. Lond. Ser. Math. Phys. Sci. 237, 212–232.

Feng, R., Yuan, W., Sextos, A., 2021. Probabilistic loss assessment of curved bridges considering the effect of ground motion directionality. Earthq. Eng. Struct. Dyn. 50, 3623–3645. https://doi.org/10.1002/eqe.3525

Flinn, E.A., 1965. Signal analysis using rectilinearity and direction of particle motion. Proc. IEEE 53, 1874–1876. https://doi.org/10.1109/PROC.1965.4462

Girmay, N., Miranda, E., 2026. Component-To-Component Variability of Response Spectral Ordinates from Strike-Slip Earthquakes. Earthq. Spectra 42, e70045. https://doi.org/10.1002/esp4.70045

Girmay, N., Miranda, E., Poulos, A., 2024. Orientation and intensity of maximum response spectral ordinates during the December 20, 2022 Mw 6.4 Ferndale, California earthquake. Soil Dyn. Earthq. Eng. 176, 108323.

Girshick, M.A., 1941. The Distribution of the Ellipticity Statistic Le when the Hypothesis is False. Terr. Magn. Atmos. Electr. 46(4), 455–457. https://doi.org/10.1029/TE046i004p00455.

Kotha, S.R., Cotton, F., Bindi, D., 2019. Empirical Models of Shear-Wave Radiation Pattern Derived from Large Datasets of Ground-Shaking Observations. Sci. Rep. 9, 981. https://doi.org/10.1038/s41598-018-37524-4

Lagaros, N.D., 2010. The impact of the earthquake incident angle on the seismic loss estimation. Eng. Struct. 32, 1577–1589. https://doi.org/10.1016/j.engstruct.2010.02.006

Lanzano, G., Luzi, L., Cauzzi, C., Bienkowski, J., Bindi, D., Clinton, J., Cocco, M., D'Amico, M., Douglas, J., Faenza, L., Felicetta, C., Gallovic, F., Giardini, D., Ktenidou, O., Lauciani, V., Manakou, M., Marmureanu, A., Maufroy, E., Michelini, A., Özener, H., Puglia, R., Rupakhety, R., Russo, E., Shahvar, M., Sleeman, R., Theodoulidis, N., 2021. Accessing European Strong-Motion Data: An Update on ORFEUS Coordinated Services. Seismol. Res. Lett. 92, 1642–1658. https://doi.org/10.1785/0220200398

Mauchly, J.W., 1940. Significance Test for Sphericity of a Normal n-Variate distribution. Ann. Math. Statist. 11 204 - 209. https://doi.org/10.1214/aoms/1177731915

Muirhead, R.J., 2009. Aspects of multivariate statistical theory. John Wiley & Sons.

Nievas, C., Sullivan, T., 2018. A multidirectional conditional spectrum. Earthq. Eng. Struct. Dyn. 47, 945–965. https://doi.org/10.1002/eqe.3000

Nievas, C.I., Sullivan, T.J., 2017. Accounting for directionality as a function of structural typology in performance-based earthquake engineering design. Earthq. Eng. Struct. Dyn. 46, 791–809. https://doi.org/10.1002/eqe.2831

Pischiutta, M., Salvini, F., Fletcher, J., Rovelli, A., Ben-Zion, Y., 2012. Horizontal Polarization of Ground Motion in the Hayward Fault Zone at Fremont, California: Dominant Fault-High-Angle Polarization and Fault-Induced Cracks. Geophys. J. Int. 188, 1255–1272. https://doi.org/10.1111/j.1365-246X.2011.05319.x

Poulos, A., Miranda, E., 2022. Probabilistic Characterization of the Directionality of Horizontal Earthquake Response Spectra. Earthq. Eng. Struct. Dyn. 51, 2077–2090. https://doi.org/10.1002/eqe.3654

Poulos, A., Miranda, E., 2021. Relations between MaxRotD50 and Some Horizontal Components of Ground-Motion Intensity Used in Practice. Bull. Seismol. Soc. Am. 111, 2167–2176. https://doi.org/10.1785/0120200364

Poulos, A., Miranda, E., Baker, J.W., 2021. Evaluation of Earthquake Response Spectra Directionality Using Stochastic Simulations. Bull. Seismol. Soc. Am. 112, 307–315. https://doi.org/10.1785/0120210101

Rupakhety, R., 2026. When Rotation-Invariant Spectra Enter Structural Design: Interpreting RotD100 and Related Measures. Earthq. Spectra 42, e70081. https://doi.org/10.1002/esp4.70081

Rupakhety, R., Hernández-Aguirre V.M., 2026. Directional peak factors of strong-motion response spectra: a stochastic field representation on the circle. Bulletin of Earthquake Engineering. https://doi.org/10.1007/s10518-026-02613-7

Shahi, S.K., Baker, J.W., 2014. NGA-West2 Models for Ground Motion Directionality. Earthq. Spectra 30, 1285–1300. https://doi.org/10.1193/040913EQS097M

Skoulidou, D., Romão, X., Franchin, P., 2019. How is collapse risk of RC buildings affected by the angle of seismic incidence? Earthq. Eng. Struct. Dyn. 48, 1575–1594. https://doi.org/10.1002/eqe.3214

Touzi, R. and Lopes, A., 1996. Statistics of the Stokes parameters and of the complex coherence parameters in one-look and multilook speckle fields. IEEE Trans. Geosci. Remote Sens. 34(2), 519-531.https://doi.org/10.1109/36.485128

Vanmarcke, E.H., 1972. Properties of Spectral Moments with Applications to Random Vibration. J. Eng. Mech. Div. 98, 425–446. https://doi.org/10.1061/JMCEA3.0001593

Vidale, J.E., Bonamassa, O., Houston, H., 1991. Directional site resonances observed from the 1 october 1987 whittier narrows, california, earthquake and the 4 october aftershock. Earthq. Spectra 7, 107–125. https://doi.org/10.1193/1.1585616